University of Huddersfield Repository

Palmer, Edward, Mishra, Rakesh and Fieldhouse, John D.

A computational fluid dynamic analysis on the effect of front row pin geometry on the aerothermodynamic properties of a pin-vented brake disc

Original Citation

This version is available at http://eprints.hud.ac.uk/id/eprint/4395/

http://eprints.hud.ac.uk/

A computational fluid dynamic analysis on the effect of front row pin geometry on the aerothermodynamic properties of a pin-vented brake disc

E Palmer, R Mishra*, and **J Fieldhouse**
Department of Engineering and Technology, University of Huddersfield, Queensgate, Huddersfield, UK

Abstract: Increasing demand from the consumer for higher levels of refinement from their passenger vehicles has put considerable pressure on the automotive industry to produce ever quieter cars. In order to prevent the occurrence of many forms of brake noise, especially judder and drone, excessive heating of the brake disc must be avoided, while minimizing temperature variations across the rotor. In order for this to be achieved the brake rotor must be designed such that it ensures sufficient uniform heat dissipation and thermal capacity. In high-demand braking applications, vented discs consisting of two rubbing surfaces separated by straight radial vanes are normally employed, as they utilize a greater surface area to dissipate heat. Within this paper the effects of changing the geometry of the first row of pins on aerothermo-dynamic properties of a pin-vented brake rotor are investigated using computational fluid dynamics (CFD). The validated CFD model shows that decreasing the thickness of the first row of pins by 10 per cent improves the mass flowrate through the rotor by 14 per cent and the heat transfer rate by 6 per cent. The results obtained can be used for the design of brake discs which are efficient with respect to heat dissipation.

Keywords: brake disc, heat transfer, CFD

1 INTRODUCTION

Owing to the increased refinement of passenger vehicles the expectations and demands of the consumer have risen. This has put greater demand on the automotive industry to produce ever quieter cars, which requires considerable effort in the area of brake refinement. Among the different types of brake noise, judder is now regarded as the most significant of all brake problems, accounting for 75 per cent of brake refinement issues [1]. This translates to a cost to the industry of $100 million (USD) per year in warranty claims alone, so the magnitude of this problem is evident [2].

The mechanism of judder is a forced vibration with a frequency directly related to the wheel speed. The vibration emanates from a variation in brake pressure caused by circumferential disc thickness variations, resulting in high-amplitude vibrations of the wheel hub and suspension system. This vibration translates to the driver and occupants as a strong pulsation of the brake pedal, which can be accompanied by vibration of the steering wheel and floor pan of the vehicle leading to a 'drumming' or 'droning' sound within the cabin. Judder may be categorized as cold or hot judder, but by far the most complex is hot judder. The circumferential disc thickness variation which results in the hot judder is caused by the thermal deformation of the rotor or an effect known as 'hot spotting' [3]. It is evident that, to prevent the occurrence of hot judder, excessive heating of the brake disc must be avoided while minimizing temperature variations across the rotor. In order for this to be achieved the brake rotor must be designed to ensure sufficient uniform heat dissipation and thermal capacity [4].

It has been shown that in a braking event the rotor may absorb approximately 90 per cent of the energy

*Corresponding author: Department of Engineering and Technology, University of Huddersfield, Queensgate, Huddersfield, West Yorkshire, HD1 3DH, UK. email: r.mishra@hud.ac.uk

[5], which generates significant temperature rise within the rotor. In high-demand braking applications vented discs are normally employed, as they utilize a greater surface area to dissipate heat. The cooling efficiency of ventilated brake discs depends on two key characteristics: the mass flowrate through the disc (i.e. the pumping efficiency of the rotor) and the average heat transfer coefficient on the surface of the disc [6]. Traditionally ventilated rotors have consisted of two rubbing surfaces separated by straight radial vanes as shown in Fig. 1(a). The thermal dissipation characteristics of a ventilated rotor can be enhanced by using curved vanes within the brake disc, thereby increasing the mass flowrate through the rotor [7]. However, use of curved vanes requires the left and right side discs to be the mirror images of each other to achieve greater pumping efficiency. Another possible means of increasing the heat dissipation of vented rotors is the use of pin-vented discs, which separate the two rubbing surfaces using a series of tear-drop and diamond sectioned columns and pillars instead of radial vanes [6]. The pumping efficiency of pin-vented rotors is less than that of a rotor with traditional vanes. However, Wallis *et al.* [8] have shown that the pin-vented discs have similar heat transfer rate when compared with discs having curved vanes because of increase in turbulence and hence heat transfer coefficient. Other advantages of these discs [8] include a higher resistance to thermal deformation owing to the more even distribution of material, which results in lower thermal stress build-up within the rotor. It has been further shown (Barigozzi *et al.* [6]) that the presence of a caliper has less effect on the mass flowrate of a pin-vented disc when compared with a curved-vane disc.

In a pin-vented disc the geometry of the pins as well as their distribution may affect heat transfer characteristics considerably. Very little work has been reported on the optimization of the geometry of pin-vented rotors to maximize the aerothermodynamic or thermomechanical properties of such rotors. Work carried out on discs with straight radial vanes [9] has shown that a parametric approach could be used to find an optimized configuration of the vanes. It has been shown in the work that the average heat transfer coefficient of the rotor could be improved by 35 per cent over a baseline design by careful selection of geometric parameters. Therefore, it is conceivable that a similar approach could yield a significant improvement in the heat transfer coefficient of pin-vented rotors. The optimization of existing brake discs is a key part of the brake design procedure as many of the parameters defining the brake's geometry and performance are often dictated by packaging restraints (wheel diameter and offset influence rotor diameter and caliper size respectively).

The current paper attempts to define a plausible way of defining and controlling the shape of the pins within a pin-vented brake disc to investigate the effects of different pin geometries on the aerothermodynamic properties of the rotor. The parametric study is aimed at understanding the relationship between disc geometry, flow field distribution, and heat dissipation characteristics. A thorough understanding of parametric interdependence will enable the design of brake discs having robust judder resistance.

Various methods have been used in the literature to investigate flow field characteristics within brake discs. These are experimental, computational, and analytical. The experimental and analytical methods have severe limitations when applied to brake discs because of limited flow space and complex flow field. The accuracy of mass flowrate and heat dissipation predictions has been vastly improved over semi-empirical predictions by the advances in computational fluid dynamics (CFD); now commercially available codes are capable of giving highly accurate results for the flow field and cooling rate of brake discs [10–12]. The present work focuses on a three-dimensional CFD parametric study of the effect of pin geometry on flow field characteristics within a commercial disc and its variants.

2 GEOMETRIC PARAMETERS

The present work is aimed at optimizing the design of a commercially available baseline pin-vented rotor consisting of three rows of 36 'pins'. These pins are positioned so that their centre-lines are separated by $10°$, with the central row of pins offset by $5°$ to the outer and inner rows as depicted in Fig. 1(b), to give the best possible aerothermodynamic properties. Preliminary studies [13] have shown that pin profiles previously referred to as diamonds and tear-drops [8] can successfully be defined using wedges and National Advisory Committee for Aviation (NACA) four series airfoils [14] and, keeping manufacturing constraints in view, appropriate radii for casting have been added to the profiles. This method for describing the profiles of the pins allows a high level of control over the shape of the pin using only four parameters – maximum camber, position of maximum camber, thickness, and length – in the case of airfoil profiled pins, and
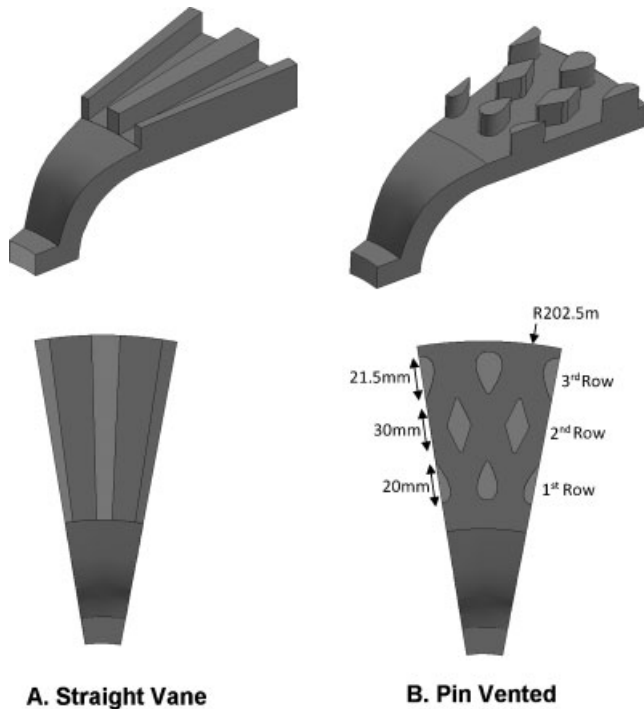
Fig. 1 Disc geometry (omitting top rubbing surface to show vane geometry)

only two parameters for wedge-shaped pins – length and thickness (defined as a percentage of the chord length) – as shown in Fig. 2. This allows the effect of changing the various parameters on the key flow field and heat transfer characteristics to be studied with relative ease.

Table 1 shows various geometries used in the present analysis. In this analysis the thickness–chord-length ratio of the airfoils and wedges has

been varied, while retaining a fixed chord length and zero degrees of camber for all pins, i.e. symmetrical airfoils. This analysis takes a baseline rotor geometry based on a commercially available pin-vented brake rotor, consisting of a first row with a NACA0050 profile, second row with a 40 per cent wedge profile, and a third row with a NACA0060 profile. The thickness–chord-length ratio of the profile of the pins in the first row is varied by ± 20 per cent from the baseline design, to find an optimized pin thickness for this row. The first row is selected for analysis as it has the greatest effect on the overall flow field distribution within the rotor, because the wake from the first row of pins affects the flow field around the pins downstream.

3 NON-DIMENSIONAL PARAMETERS

It is proposed to evaluate the flow field in the present investigation with the help of non-dimensional numbers to eliminate the effect of scale. The definition of the non-dimensional parameters used is given below.

Dimensionless radius: the dimensionless radius is defined as the radial distance between the centre of the brake rotor and the point of interest, divided by the outer radius of the rotor.

$$r_d = \frac{r}{R}$$

Dimensionless channel width: the non-dimensional channel width is a measure of the distance between
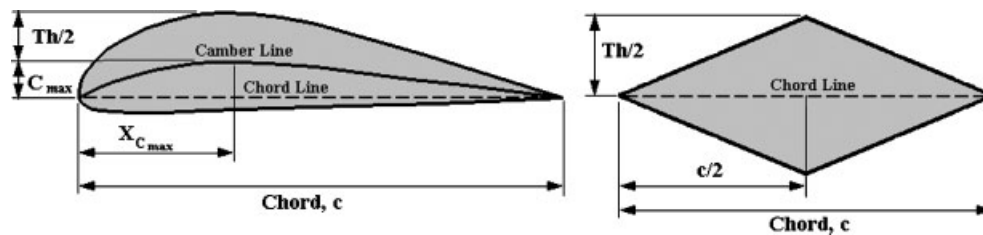
Fig. 2 Pin geometry

Table 1 Analysis geometry

Design	First row profile	First row frontal area (mm^2)	Second row profile	Third row profile
1	NACA0030	72	Wedge40%	NACA0060
2	NACA0040	79.2	Wedge40%	NACA0060
3	NACA0045	86.4	Wedge40%	NACA0060
4	NACA0050	93.6	Wedge40%	NACA0060
5	NACA0055	96	Wedge40%	NACA0060
6	NACA0060	108	Wedge40%	NACA0060
7	NACA0070	120	Wedge40%	NACA0060

the pins from the pressure side to the suction side of the pins within a row. It is defined as the circumferential distance between the pressure side of the pin and the point of interest, divided by the total circumferential distance between the pins (Fig. 3)

$$\alpha' = \frac{\alpha}{\alpha_{\mathrm{o}}}$$

Dimensionless relative velocity: the dimensionless relative velocity is defined as a ratio of the relative velocity at the point of interrogation and the linear velocity at the outer diameter of the brake disc. In the above the relative velocity at the point of interest is defined as the difference between the flow field velocity vector and the linear vector of the rotating domain at the point of interest.

$$\bar{V}_{\mathrm{rel}} = \frac{V_{\mathrm{rel}}}{\omega R}$$

4 MATHEMATICAL FORMULATION

The CFD programs employ a mathematical model to simulate a physical flow field. This includes a set of partial differential equations and boundary conditions. The CFD package Fluent solves Navier–Stokes equations, along with the continuity equations and appropriate auxiliary equations depending on the type of application, using a control volume formulation. In the present case the conservation equations for mass, momentum, and energy have been solved
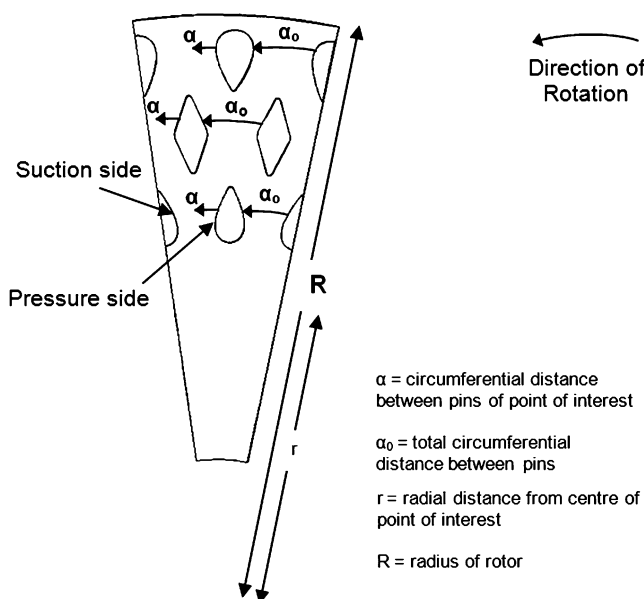

Fig. 3 Non-dimensional geometric parameters

with two additional flow transport equations for steady turbulent flow [15].

Fluent uses the finite volume method to solve the Navier–Stokes equations and is known for its robustness in simulating many fluid dynamic phenomena. The finite volume method consists of three stages. First is the formal integration of the governing equations of the fluid flow over all the (finite) control volumes of the solution domain. Then comes discretization, involving the substitution of a variety of finite-difference-type approximations for the terms in the integrated equation representing flow processes such as convection, diffusion, and sources. This converts the integral equation into a system of algebraic equations, which can then be solved using iterative methods [16]. The first stage of the process, the control volume integration, is the step that distinguishes the finite volume method from other CFD methods. The statements resulting from this step express the 'exact' conservation of the relevant properties for each finite cell volume.

To enable the modelling of a rotating body (in this case the disc) the code employs the rotating reference frame technique. This technique employs a modified version of the momentum and conservation equations. In terms of absolute velocities the left-hand side of the momentum equations becomes

$$\frac{\partial}{\partial t}(\rho \boldsymbol{v}) + \nabla \cdot (\rho \boldsymbol{v}_{\mathrm{r}} \boldsymbol{v}) + \rho (\boldsymbol{\Omega} \times \boldsymbol{v})$$

$\boldsymbol{v}_{\mathrm{r}}$ is defined as relative velocity and $\boldsymbol{\Omega}$ is the angular velocity vector. The continuity equation employed in rotating reference-frame problems is written as

$$\frac{\partial \rho}{\partial t} + \nabla \cdot (\rho \boldsymbol{v}_{\mathrm{r}}) = S_{\mathrm{m}}$$

The implementation of periodic boundary (cyclic symmetry) conditions meant that only a periodically repetitive 20° section of the disc was modelled rather than the whole disc. This had the effect of making the model much smaller, translating to lower hardware requirements, and saving vast amounts of computational time.

The disc was modelled as rotating in still air by implementing atmospheric temperature and pressure at the inlet and outlet boundaries. The walls of the disc are represented as smooth walls at a constant temperature of 800 K. Although this is a massive simplification of most real-life braking events it is deemed an adequate method for the simulation of brake discs in CFD for the sake of design comparison [**8, 10, 11**]. Symmetry boundary

Table 2 Boundary conditions

| Boundary	Boundary condition	Parameters
Inlet	Pressure inlet	Atmospheric pressure and temperature
Outlet	Pressure outlet	Atmospheric pressure and temperature
Domain edges	Symmetry	Symmetry
Disc surface	Wall	800 K temperature, thermal properties of grey cast iron

conditions have been used to generate zero-shear slip walls at the edge of the domain [10].

The speeds of rotation for the simulation range from 500 to 2000 r/min correlating to approximately 25–100 per cent of maximum vehicle speed of a high-performance passenger car. As radiation and conduction to the hub are neglected within the simulation, higher speeds of rotation were chosen because previous work has shown that convective cooling becomes the predominate medium of heat transfer at rotation speeds above 500 r/min [17]. A complete summary of the boundary conditions used is given in Table 2 and shown in Fig. 4.

The Reynolds number over the first row of pins is calculated from the inlet velocity obtained using the equation proposed by Limpert [18] (see below), with a minimum value of 5.96×10^4 for 500 r/min and a maximum value of 9.53×10^5 obtained for 2000 r/min; hence turbulent flow has been assumed to take place within the disc

$$V_{in} = 0.170604n\left(D_o^2 - D_i^2\right)$$

In order to model the turbulence the semi-empirical standard K–ε turbulence model with standard wall treatments is employed in this study, as it has been shown to give accurate flow predictions in previous work [10–12]. A mesh independence analysis as well as volume mesh optimization were carried out, and
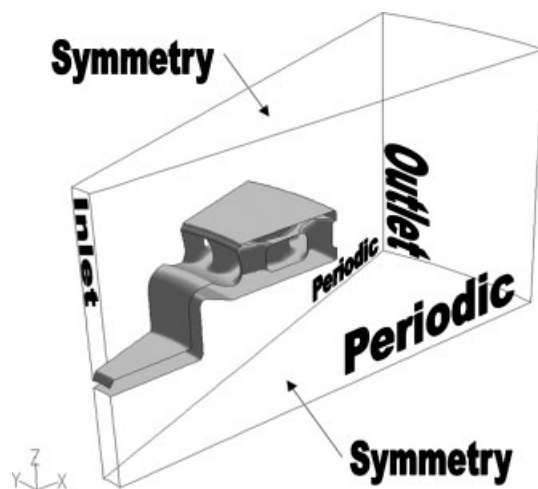
the final mesh structure consists of a fine mesh near the walls of the disc and a coarse mesh near the boundaries of the domain. It was seen that the results became independent of the mesh spacing when approximately 1.3 million tetrahedral elements were used in the flow domain. The mesh convergence analysis was performed on a model with an initial mesh of approximately 500 000 elements. The density of the mesh applied to the edges of the model was increased by a factor of 1.2 until a mesh-independent solution was obtained. The standard relaxation factors were applied with convergence criteria of 0.0001 for all residuals as recommended by the Fluent manual [15] for a tight convergence. A second-order up-wind discretization scheme is utilized as part of the solution regime for greater accuracy at the cell faces. The study was performed on an AMD 3800+ Athlon 64 machine with 2 GB of system RAM using a steady state solution scheme in a run time of approximately 10 h for each of the design iterations.

5 VALIDATION OF COMPUTATIONAL APPROACH

Computational fluid dynamics is an approximate solution technique used in the prediction of flow fields. The accuracy of results from CFD simulations depends on the quality of the mesh and the user's ability to utilize the correct modelling techniques within the solver. Therefore validation of results obtained from the CFD analysis is essential to make meaningful predictions. In the present work the CFD model has been validated from the data available in the literature. Most of the available literature do not give the exact geometric details of the rotors analysed, making the application of the results for the purpose of validation difficult. Nevertheless geometric details of the discs studied by Wallis *et al.* [8] are available. This paper details a CFD comparison of pin and radial vane ventilated rotors; the techniques employed in this study are later validated experimentally using particle image velocimetry in further work by the same author [19], where a strong correlation can be seen between the experimental and computational results for

Fig. 4 CFD boundary conditions

pin-vented rotors. Therefore, it is possible to validate the CFD techniques employed in this paper against the experimental data obtained by Wallis by comparing results obtained for the same rotor geometry.

Figure 5 depicts the locations at which simulated results have been compared against the experimental data. The flow fields are compared along two radial lines positioned $\pm 2.5°$ from the centre-line of the second pin at 50 per cent of the passage height.

The comparison of the results for non-dimensional relative velocity distribution presented in reference [19] with those obtained in the present study for the locations along the first line is shown in Fig. 6. The graph shows that there is generally
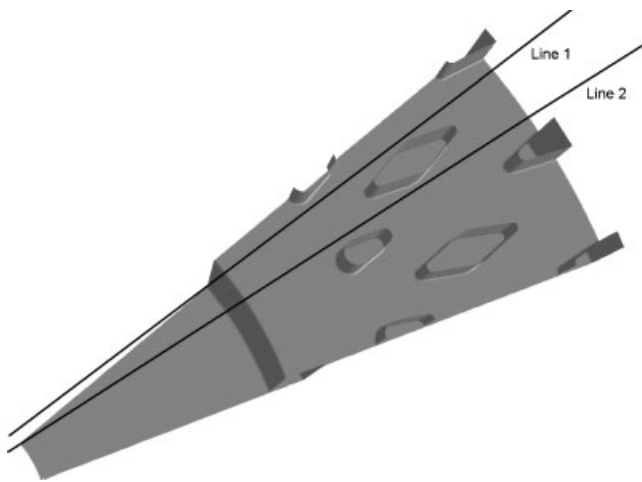

Fig. 5 Lines of investigation for comparison of CFD models

good qualitative agreement between the two sets of results. The non-dimensional velocity is seen to increase up to a radius ratio of 0.4 in both cases, beyond which it suddenly drops because of the presence of the first row of pins. There is only marginal difference between the two sets of results up to a radius ratio of 0.5, beyond which Wallis's results tend to be greater than those obtained from the present study up to a radius ratio of 0.6. The largest discrepancy between the two data sets can be seen at radius ratio 0.7, where the results obtained by Wallis show a much larger peak in the relative velocity magnitude than those from the CFD model. Beyond radius ratio 0.75 the two cases give almost identical values. Overall difference between the two relative velocity values is calculated to be 5 per cent, with an average deviation of 0.3.

The comparison of the non-dimensional velocity distribution for the second line of investigation is presented in Fig. 7. As with the first line there is generally a strong correlation between the results obtained by Wallis and those from the computational model used in the present study. The non-dimensional relative velocity increases up to a radius ratio of 0.5 where both sets of data show a drop in relative velocity value because of the presence of a stagnation point on the high-pressure side of the first row of pins. Both sets of results then show an increase in relative velocity value until a radius ratio value of 0.55. However, beyond this point a sudden drop in relative velocity is noticed, which has been caused by the wake created behind the second row of pins. There is some difference in the relative
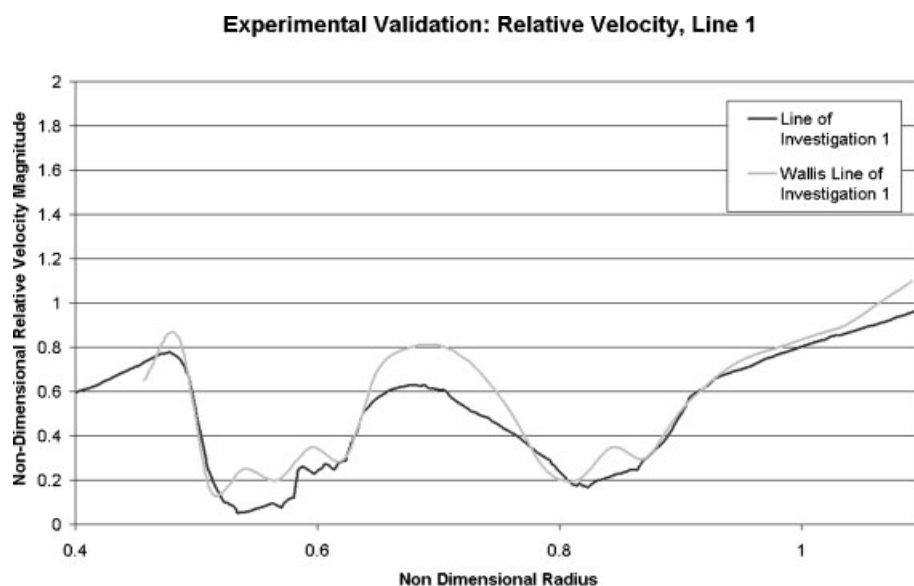
Fig. 6 Quantitative comparison of relative velocity magnitude, line 1
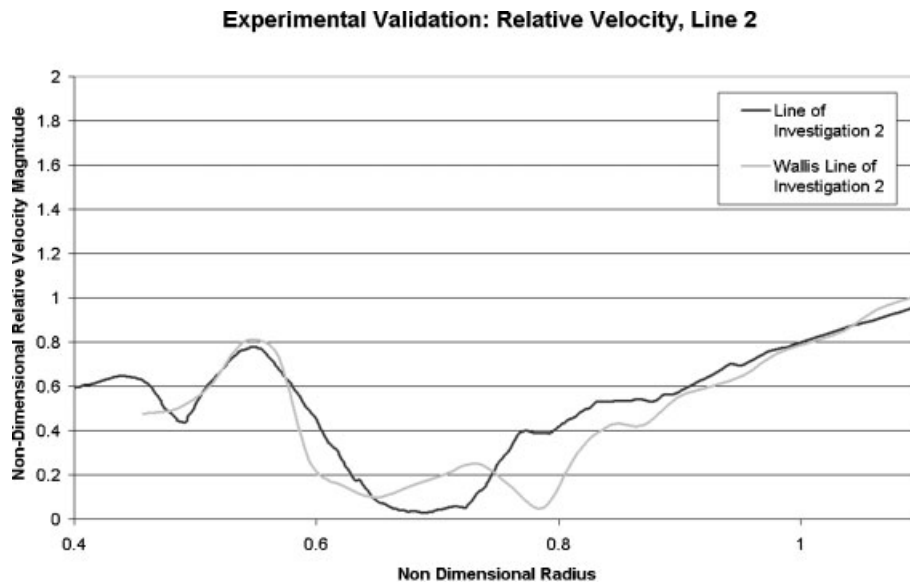
Fig. 7 Quantitative comparison of relative velocity magnitude, line 2

velocity values at the locations corresponding to the wake trailing the second row of pins. However, the overall difference between the two relative velocity values is 1.5 per cent with an average deviation of 0.3.

It can be concluded from the above discussion that the level of qualitative similarity obtained in the flow patterns in the two analyses is good. Localized differences between the results can be attributed to the limitations of the K–ε model. It also worth noting that there is an error factor of approximately ± 0.05 in results given for Wallis as they have been taken from contour plots [**19**]. Further inaccuracies might have crept in to Wallis's work because of the numerical interpolation scheme used to convert raw data into contour plots. Although some discrepancies have been seen, the overall agreement between the two data sets is sufficiently acceptable to assume that the modelling technique is valid.

6 RESULTS

6.1 Results for baseline disc

After validating the CFD model, the flow through a commercially available pin-vented brake disc has been analysed. Figure 8 displays the flow field within the baseline brake rotor. Various flow field characteristics such as static pressure distribution, temperature distribution, and relative velocity field, which have a strong influence on heat transfer characteristics, have been depicted in this figure. The variation of static pressure over the flow field is

shown in Fig. 8(a). It clearly shows the formation of high static pressure regions at the front of the first and second rows of pins. A considerable variation in static pressure values is seen across the disc. The static pressure value reaches a minimum of -1570 Pa at radius ratio of 0.627 (labelled 'Min') on the trailing edge of the first row of pins whereas the maximum static pressure value is 568 Pa at a radius ratio of 0.65 (labelled 'Max') on the high-pressure side of the first row of pins. The pressure field indicates that the presence of pins causes a considerable variation in pressure magnitudes.

In order to analyse the flow pattern and its likely correspondence with pressure field, the relative velocity profile at 50 per cent of the passage height is depicted in Fig. 8(b). It can be seen that the relative velocity magnitudes also change over a wide range of values. The maximum relative velocity obtained in this analysis is 44.42 m/s, recorded at a radius ratio of 0.627 on the trailing edge of the first row of pins. This location corresponds to the position of minimum pressure as well. This figure also clearly shows the regions of separated flow following each pin. Figure 8(c) shows the corresponding path line plot within the disc. From this diagram it can be seen that the separated flows following each pin form regions of recirculation. This also indicates that the presence of pins complicates the flow pattern inside the disc. Figure 8(d) shows the temperature distribution, which clearly indicates that the regions where flow has separated act like hot spots with very high temperatures. A comparison of Figs 8(b) and (d) also shows that the region of lowest velocity corresponds to the
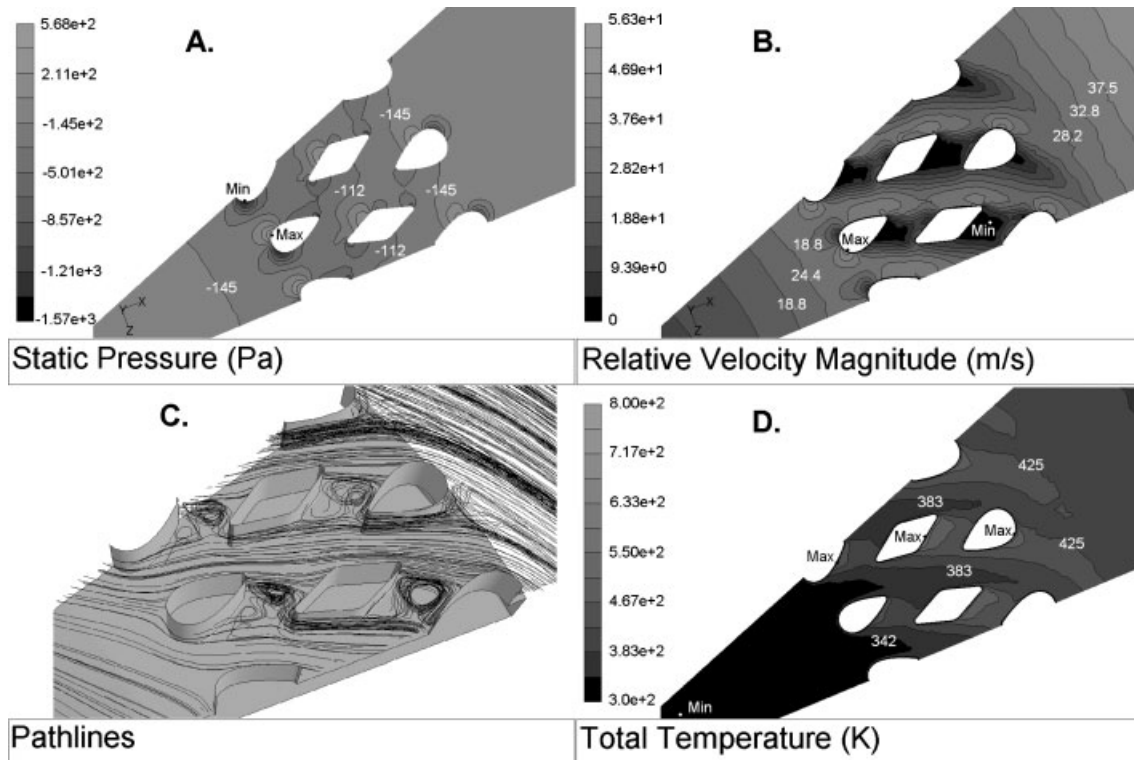
Fig. 8 Flow field characteristics for a pin-vented rotor

regions of highest temperature on the trailing edge of the second and third rows of pins. In these regions the temperature is 512 K, while the minimum temperature is 300 K, giving a temperature ratio (ratio of maximum temperature to minimum temperature) of 1.70.

To quantify the effect of the above flow parameters on the cooling characteristics, mass flowrate at the exit of a 20° section of the disc has

been computed within the Fluent package to be 0.0026 kg/s, equating to a mass flowrate through a complete rotor of 0.0468 kg/s.

Contours of heat transfer coefficient extracted from the CFD study are presented in Fig. 9 to show the relationship between the flow field characteristics presented in Fig. 8 and the heat transfer properties of the rotor. The distribution of heat transfer coefficient over the disc is non-uniform,
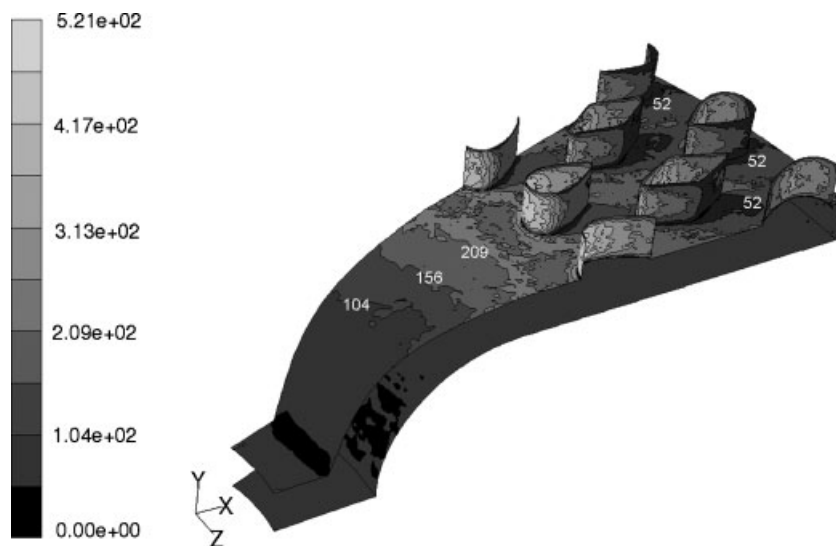

Fig. 9 Heat transfer coefficient distribution on the disc surface $(W/m^2 K)$

with troughs in the low-velocity regions and peaks in the high-velocity regions. This is because high-energy dissipation occurs in the high-velocity regions and low-energy dissipation in the low-velocity regions. The heat transfer coefficient values vary from approximately $520\,\mathrm{W/m^2\,K}$ on the high-pressure side of the first row of pins to just below $60\,\mathrm{W/m^2\,K}$ on the trailing edge of each row of pins, resulting in an average heat transfer coefficient of $125.4\,\mathrm{W/m^2\,K}$ and heat transfer rate of $32.35\,\mathrm{kW}$ over the entire rotor. The large variations in heat transfer coefficient are common for pin configurations [13]. It can therefore be seen that in a pin-vented disc the heat transfer coefficients vary over a wide range when compared with those generated for a straight-vane-type disc, where the local heat transfer coefficients tend to vary by around 100 per cent.

6.2 Optimization of first row pin geometry

The direction of flow in a vented disc is radially outwards. Hence geometric features near the centre of the disc are likely to have a strong influence on mass flowrate and hence heat transfer characteristics of the disc. In the present study, therefore, the effect of front row pin geometry, as detailed in section 2 of this paper, on mass flow and heat transfer characteristics has been investigated.

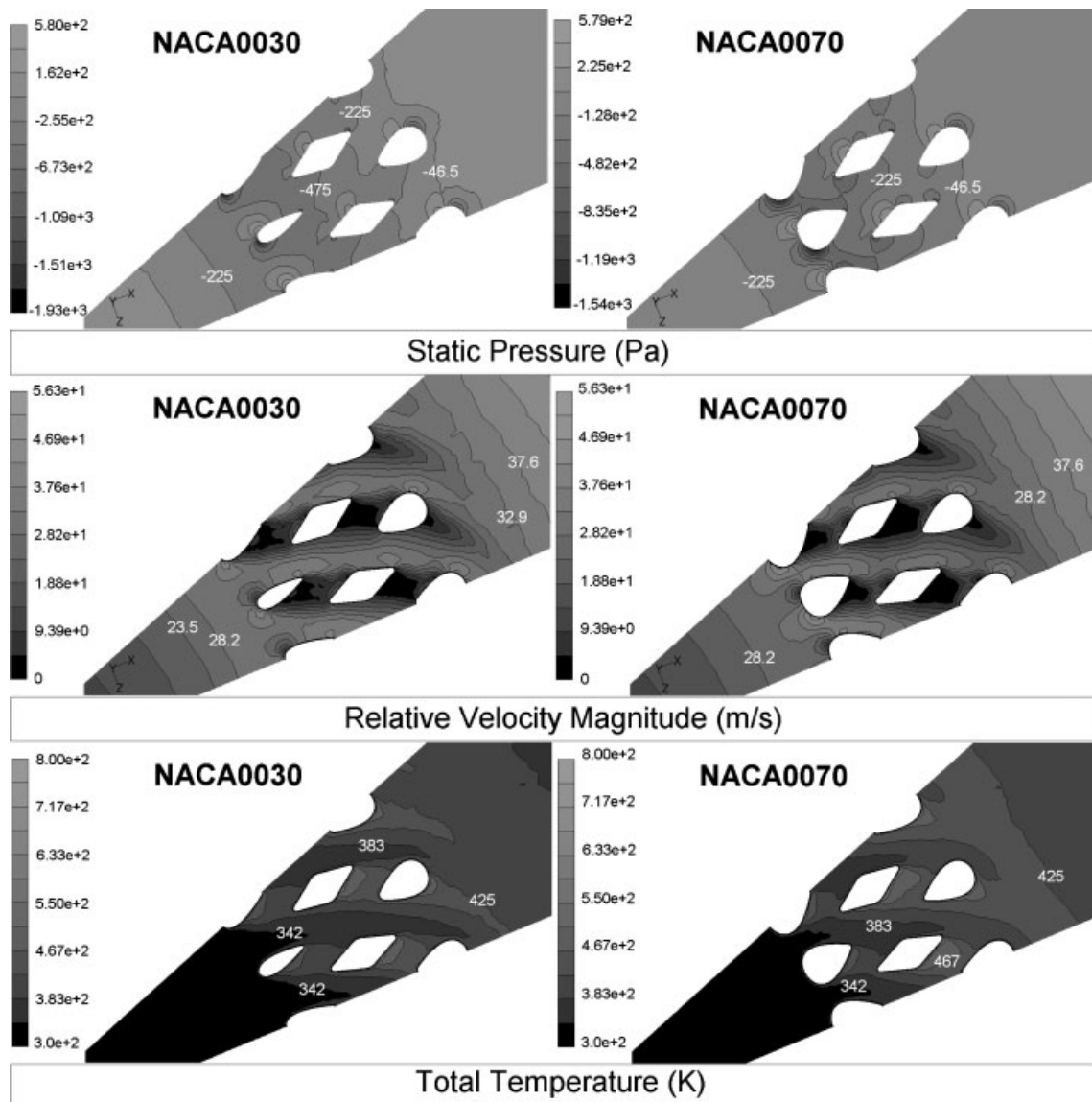Figure 10 displays the effect of first row pin thickness on the static pressure and temperature

Fig. 10 Contours of static pressure, turbulence intensity, and relative velocity magnitude at 50 per cent channel height

distribution as well as the relative velocity magnitude. In order to establish clearly the effect of front row pin thickness, the results obtained from two pin geometries widely differing in thickness (NACA0030 and NACA0070) have been presented. The variation in static pressure distribution shows that, as with the baseline disc, both modified geometries generate regions of high pressure on the high-pressure side of the first and second rows of pins and a region of low pressure on the trailing edge of the first row. The NACA0030 profile generates a maximum static pressure of 566 Pa at a radius ratio of 0.627, equating to a 0.3 per cent decrease when compared with the baseline rotor. The minimum static pressure produced by the NACA0030 profile pins is −1930 Pa on the trailing edge of the first row of pins at a radius ratio of 0.645, which is equal to a 23 per cent decrease when compared with the baseline disc. At a radius ratio of 0.600, the NACA0070 profile produces a maximum static pressure of 579 Pa, a 2 per cent increase over the baseline rotor. The value of minimum pressure generated by NACA0070 profile is −1540 Pa at the same radius ratio, equating to a 2 per cent increase over the baseline design. It can be concluded from the above discussion that the profile of the first row of pins has a marginal effect on the maximum static pressure developed on the high-pressure side, whereas considerable variation is seen in the minimum pressure value. Decreasing thickness of the pin results in lower minimum pressure values.

Figure 10 also depicts the relative velocity contours within the discs under investigation. As with the baseline rotor, the velocity profiles for the modified geometries vary over a wide range of values. The change in maximum and minimum relative velocity values is negligible between the modified geometries and the baseline rotor. However, there is significant change in the velocity distribution. The NACA0070 profile rotor creates a larger region of high velocity on the trailing edge of the pin and higher velocities at the inlet when compared with the baseline and NACA0030 profile rotors. The NACA0030 profile rotor generates higher velocities upstream of the inlet in comparison with the baseline and NACA0070 rotors owing to reduced upstream blockage. A larger region of high velocity after the stagnation point on the high-pressure side of the first row of pins can also be noticed, leading to a much larger region of high velocity along the high-pressure side of the second and third rows of pins.

The temperature plot shows that higher velocities along the high-pressure faces of the pins give rise to lower temperatures in these regions compared with the NACA0070 and baseline rotors (more detailed description is required in terms of maximum and minimum values).

It can be concluded from the above discussion that increasing pin thickness has a large effect on the flow field within the discs. To analyse the above in more depth, static pressure distribution has been analysed at three sections, as shown in Fig. 3. Figure 11 depicts the static pressure distribution between the pins in the first row, at a radius ratio of 0.66 for all the rotor variants. It can be seen that for the baseline profile the static pressure values increase on moving away from the pin pressure side and then start to decrease again towards the suction side. For this disc the static pressure value at a non-dimensional channel width dimension of 0.1 (taken in an anti-clockwise direction) is −515 Pa. The static pressure then increases across the channel width to a maximum of −405 Pa at a channel width of 0.375; after this there is a decrease in static pressure to −492.5 Pa at a channel width of 0.875. Therefore, the overall change in static pressure across the channel width is 4.4 per cent. Figure 11 clearly shows that increasing thickness of the pin results in lower pressures in the area immediately to the left of the pin (high-pressure region). The trend is opposite on the suction side of the next pin, although differences in magnitudes are not high. It can also be seen from Fig. 11 that the NACA0030 profile pin generates a maximum static pressure of −373.1 Pa and a minimum static pressure of −586.1 Pa, resulting in a 57 per cent decrease in the static pressure across the channel width. The average static pressure across the vane gap is calculated to be −485.6 Pa, whereas the NACA0070 profile pin generates a maximum static pressure of −464.2 Pa on the trailing edge and a minimum static pressure of −719.9 Pa on the high-pressure side, resulting in a 55 per cent increase across the width of the channel with an average static pressure between the pins of −540.6 Pa.

It can therefore be concluded that as the pin profile is changed from the baseline design, the pressure variation between the pins in the front row shows a mixed trend. Increasing the thickness of the profile of the pins in the first row decreases the pressure in the high-pressure region (non-dimensional channel width < 0.5) of the pins. This can be attributed to the availability of less flow area resulting in higher velocities and lower pressures, whereas in the suction region of the pin (non-dimensional channel width > 0.5), increasing the pin profile width results in slightly higher static pressure.
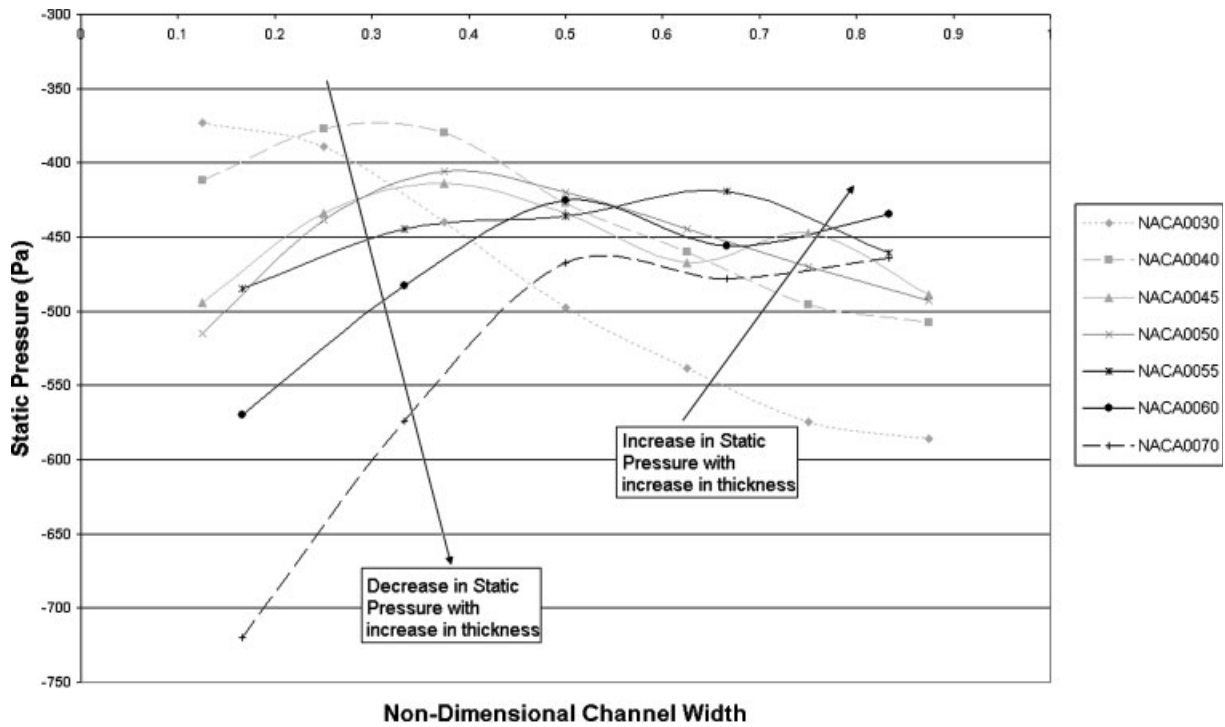
Fig. 11 Effect of first row geometry on static pressure distribution at $R = 0.66$

Figures 12 and 13 show the static pressure distribution between the pins in the second and third row respectively. For the baseline disc it can be seen that static pressure initially increases as the non-dimensional distances increase. The static pressure value peaks at a radius ratio value of 0.2 and then it starts decreasing. Similar trends are seen for all variants of the brake line disc as well. It can further be seen from Fig. 13 that an increase in the thickness of the profile of the pins in the first row generally causes an increase in the static pressure distribution across the vane gap. The trend predicts
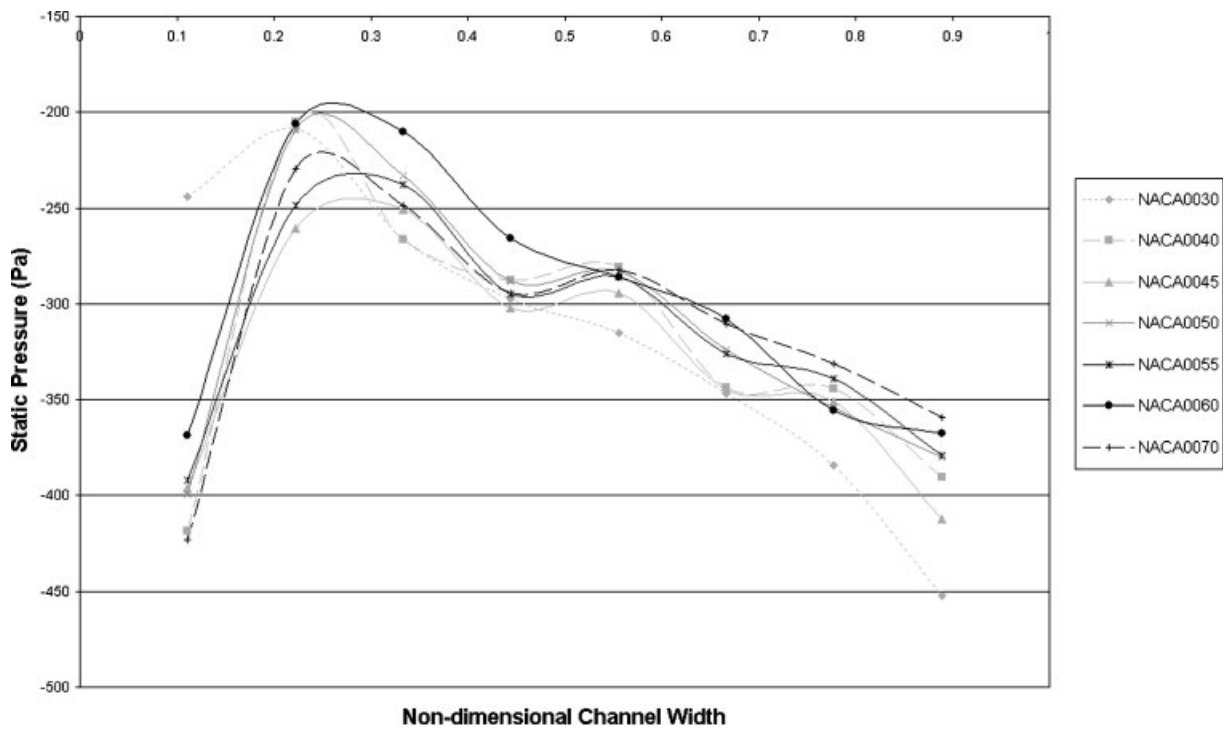

Fig. 12 Effect of first row geometry on static pressure distribution at $R = 0.8$
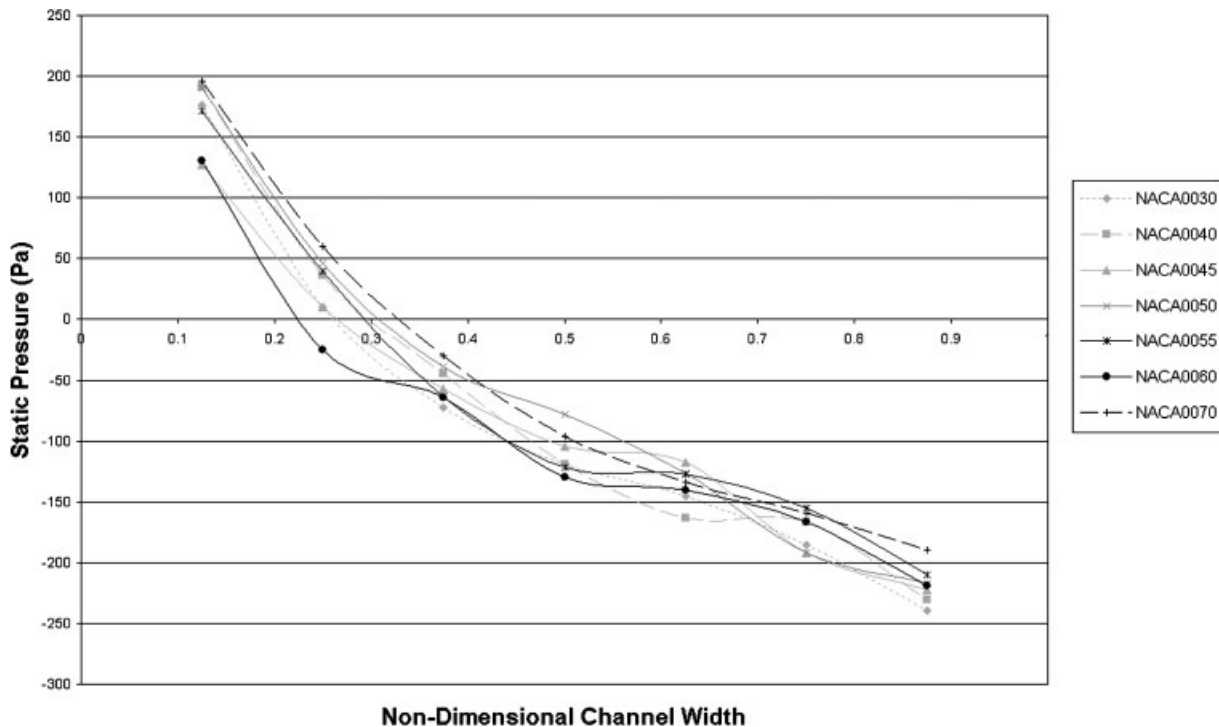
Fig. 13　Effect of first row geometry on static pressure distribution at $R = 0.92$

that there is approximately a 15 Pa average static pressure rise between the pins in the second row over the range of pin profiles. As with the second row, Fig. 13 shows that the average static pressure between the pins in the third row increases as the pin profile thickness of the first row is increased. Like the second row of pins, the trend predicts an approximate average static pressure rise between the pins of 15 Pa. From these trends it can be concluded that the thinner pin profiles promote higher mass flowrates through the rotor.

To quantify the effect of the profile of the front row pins on mass flow characteristics, a non-dimensional velocity distribution parameter has been used, which is defined as the ratio of the radial velocity component to the tangential velocity component. At a given location this parameter gives a measure of the redistribution of flow. The greater the average non-dimensional velocity distribution parameter across the width of the passage between the pins, the larger the mass flowrate through the rotor. The non-dimensional velocity distribution is analysed across the channel width between the pins at three different radii – 0.66, 0.8, and 0.92 (Fig. 3) – and is shown in Fig. 14. In order to allow the comparison, the non-dimensional velocity values have been plotted against the non-dimensional channel width.

It can be seen from Fig. 14 that for the thinnest profile of the first row of pins (NACA0030), the bulk

of the flow passes through the central 80 per cent of the pin gap with significant asymmetry in the velocity profile, with high values of non-dimensional velocity distribution parameter nearer the high-pressure side and low values of velocity parameter on the suction side at a radius of 0.66. A similar trend is seen for the NACA0070, but the extent of asymmetry is increased. At the middle location ($R = 0.8$) for both the profiles, velocity values have reduced considerably because of diffusion, and the extent of asymmetry has reduced as well. Similar trends have been noticed at a radius of $R = 0.92$ mm. Static pressure profiles seen in Fig. 11 tie in with the velocity profiles seen here. At the locations where high velocities have been seen, Fig. 11 shows that the pressure values are smaller.

The pressure and velocity fields directly affect mass flow characteristics of the disc. This section describes the effect of varying the first row pin profile on the mass flowrate of air passing through the disc at various speeds. Figure 15 clearly shows the effect of increasing the frontal area of the pin on mass flowrates through the disc. It can be seen that increase in the pin thickness results in lower mass rate of flow at a given speed.

From Fig. 15 it can also be seen that speed also has a pronounced effect on the mass flowrate through the disc. Increasing the speed of rotation results in higher flowrates of air through the disc, likely
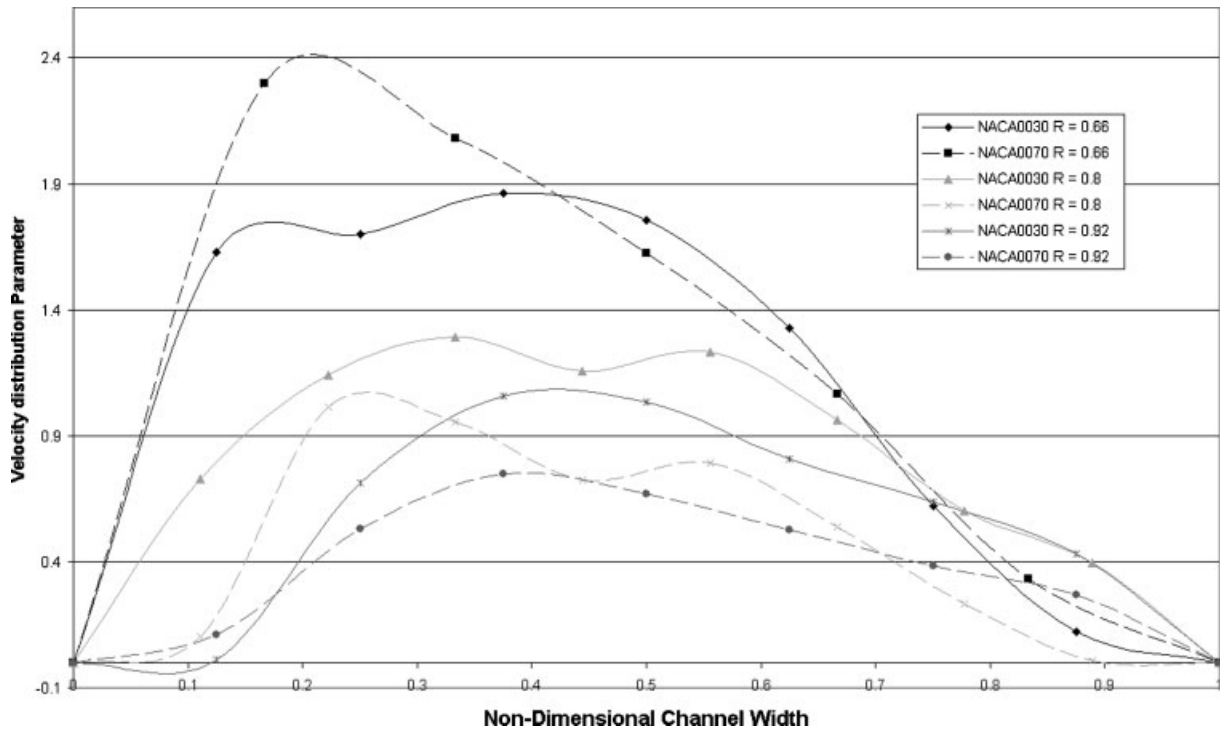
Fig. 14   Effect of first row pin geometry on non-dimensional velocity distribution parameter
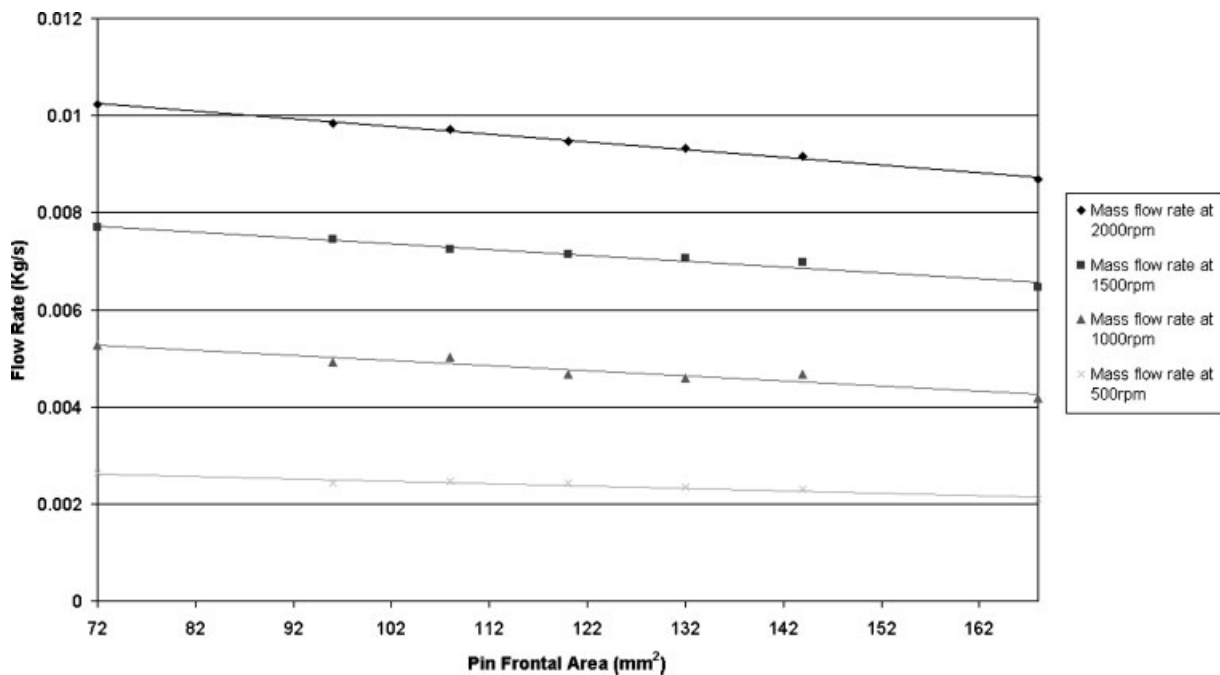

Fig. 15   Effect of first row pin thickness on mass flowrate across the range of angular velocities

resulting in higher heat transfer rates. This is in agreement with results obtained previously by Limpert [18], Sisson [20], and Wallis and co-workers [8, 19], as well as observations made by Barigozzi *et al.* [6].

In order to analyse the heat transfer characteristics, Fig. 16 has been prepared, which depicts heat

and mass flow characteristics at the maximum speed used in the present investigation of 2000 r/min. It can clearly be seen that as the pin thickness is increased the mass flowrate of air through the disc generally decreases, which results in a corresponding decrease in heat transfer rate. It can also be seen
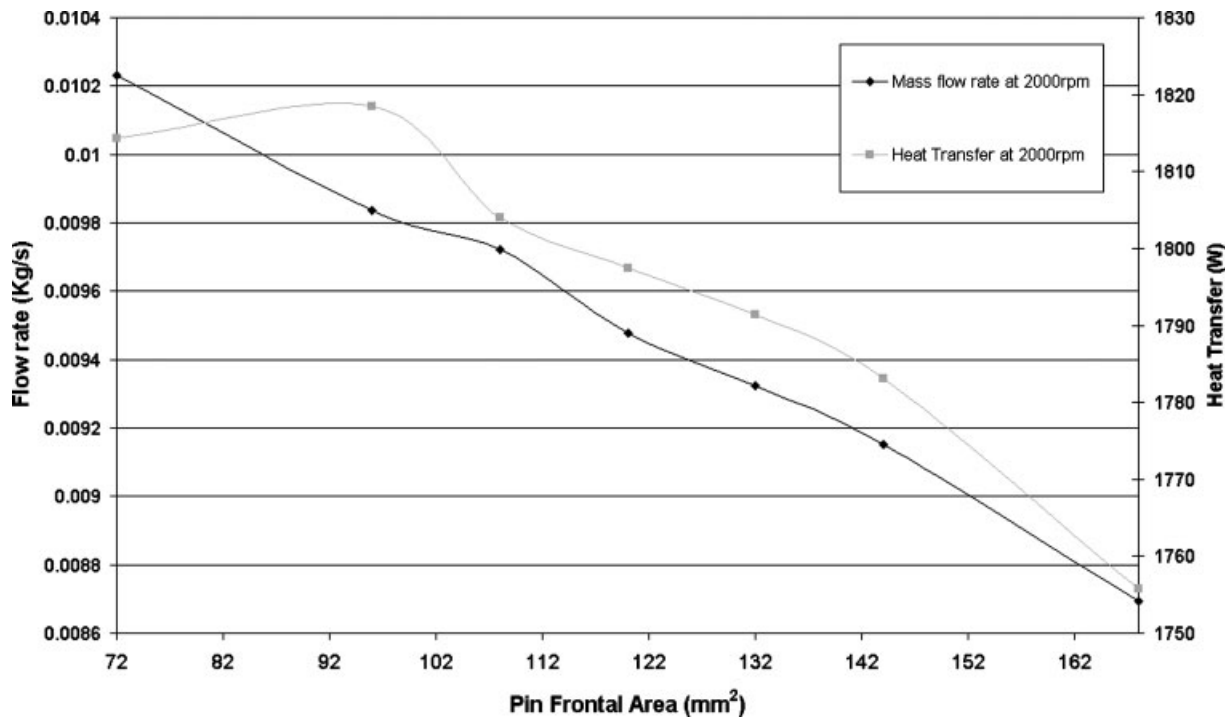
Fig. 16 Effect of first row pin thickness on mass flow and heat transfer at 2000 r/min

that the trends seen for mass flow characteristics are similar to heat transfer characteristics, indicating a strong correlation between the two until the pin profile thickness is decreased to NACA0040. In order to gain a greater understanding of what happens when the pin profile is decreased to less than NACA0040, additional models with first row pin profiles of NACA0033, NACA0036, and NACA0039 have been simulated. These points show that the mass flowrate continues to increase with a near linear relationship as the pin profile is decreased, with a maximum of 0.0102 kg/s occurring at NACA0030. The heat transfer rate, however, deviates from the previously linear trend, with a peak heat transfer rate of 1836 W observed for the NACA0036 profile; after this point the heat transfer rate begins to decrease with a decrease in pin profile. Despite the increased flow through the NACA0030 disc compared with the NACA0036, there is a reduction in the total heat transfer. There are two possible reasons for this decrease. The first is the reduction in wetted surface area for the heat to be removed from the rotor. This is in agreement with conclusions drawn by Carlos *et al.* [21], who stated the importance of maximizing wetted area and heat transfer coefficient to give optimal heat transfer characteristics. However, the reduction in wetted area between the NACA0036 profile and the NACA0030 profile is negligible (less than 0.1 per cent). Another possible explanation for the decrease in the heat transfer for pins with a slimmer profile than

NACA0036 is the increase in inlet area, which causes an increase in the mass flowrate, yet at the same time yields a decrease in the inlet velocities. This in turn reduces the heat transferred because it is well known that heat transfer is a function of the velocity; this has been described earlier as well in the comparison of Figs 8 and 9. The approximate difference between the highest and lowest mass flowrates is 14 per cent and the difference over the range of heat transfer rates is approximately 6 per cent.

7 CONCLUSIONS

The present investigation has clearly revealed that pin profiles affect heat transfer characteristics of a pin-vented disc considerably. It has been successfully shown that through control of one parameter, the pin thickness of one row, it is possible to increase the mass flowrate through the disc by 14 per cent and the heat transfer rate by 6 per cent. It was found that increasing the profile thickness resulted in a decrease in the mass flowrate through the disc and a decrease in the average non-dimensional velocity distribution parameter of the flow within the rotor. This results in a decrease in the heat transfer coefficient. In the present investigation, the NACA0030 profile has been found to give the best mass flow, and the NACA0036 has been found to have the best heat transfer characteristics.

REFERENCES

1 **Thompson, J.** State of the art towards the NVH robust brake – USA position. In Proceedings of Brakes 2006, an NVH Robust Brake Session, York, UK, 7 May 2006.

2 **Akebono Braking Technology.** Brake noise, vibration and harshness: technology driving customer satisfaction, 2005. Further information available from www.akebonobrakes.com.

3 **Steffen, T.** Hot spot simulation. In Proceedings of the IMechE Conference on Brakes 2006, York, UK, 2006, pp. 199–208.

4 **Dahm, K. L.** and **Dearnley, P. A.** Thermal modelling of disc brake rotors to enable the optimal exploitation of surface engineering. In Proceedings of the IMechE Conference on Brakes 2006, York, UK, 2006, pp. 115–124.

5 **Phan, D.** and **Kondyles, D.** Rotor design and analysis; a technique using computational fluid dynamics (CFD) and heat transfer analysis. SAE paper 2003-01-3303, 2003.

6 **Barigozzi, G., Cossali, G. E., Perdichizzi, A., Boden, A.,** and **Pacchiana, P.** Experimental investigation of the mean and turbulent flow characteristics at the exit of automotive vented brake discs. SAE paper 2002-01-2590, 2002.

7 **Massey, B. S.** *Mechanics of fluids,* 6th edition, 1989, pp. 534–538 (Chapman and Hall).

8 **Wallis, L., Leonardi, E.,** and **Milton, B.** Air flow and heat transfer in ventilated disc brake rotors with diamond and tear-drop pillars. *Numer. Heat Transfer, Part A,* 2001, **41**, 643–655.

9 **Qian, C.** Aerodynamic shape optimization using CFD parametric model with brake cooling application. SAE paper 2002-01-0599, 2002.

10 **Tirovic, M.** and **Galindo-Lopez, C. H.** Analysis of air flow and heat dissipation from wheel mounted railway brake discs. In Proceedings of the IMechE Conference on Brakes 2006, York, UK, 2006, pp. 125–134.

11 **Voller, G. P., Tirovic, M.,** and **Gibbens, P.** Analysis of automotive disc brake cooling characteristics. *Proc. Instn Mech. Engrs, Part D: J. Automobile Engineering,* 2003, **217**, 657–666.

12 **Yeo, T. I., Choi, H.,** and **Kim, J. H.** Equivalent axisymmetric finite element applied to undercut shape design of ventilated brake disk. In Proceedings of the IMechE Conference on Brakes 2006, York, UK, 2006, pp. 135–144.

13 **Palmer, E., Fieldhouse, J.,** and **Mishra, R.** Optimisation of pin shape and its configuration for a 'pin' type vented brake disc using CFD. In Proceedings of the FISITA World Automotive Congress, October 2006, paper F2006D115.

14 **Jacobs, E., Ward, K.,** and **Pinkerton, R.** The characteristics of 78 related airfoil sections from tests in the variable-density wind tunnel. In Proceedings of the NACA Conference, Yokohama, Japan, 1933, TR no. 460.

15 **Fluent Incorporated.** *Fluent user guide,* 2003 (Fluent Incorporated).

16 **Versteeg, H. K.** and **Malalasekera, W.** *An introduction to computational fluid mechanics; the finite volume method,* 1995 (Prentice Hall).

17 **Daudi, A.** and **Narain, M.** 72 curved fin rotor design reduces maximum rotor temperature. SAE paper 1999-01-3395, 1999.

18 **Limpert, R.** Cooling analysis of disc brake rotors. SAE paper 751014, 1975.

19 **Wallis, L. M.** A comparison of bi-directional disc brake rotor passage designs, Australian Digital Theses Program, 2003.

20 **Sisson, A.** Thermal analysis of vented brake rotors. SAE paper 780352, 1978.

21 **Carlos, H., Galindo, L.,** and **Tirovic, M.** Air flow and heat dissipation analysis of commercial vehicle brake discs. In Proceedings of the 11th European Automotive Congress EAEC, Budapest, Hungary, 2007, paper CV06-3.

APPENDIX

Notation

c	chord length (m)
C_{max}	maximum camber (m)
D_i	inner diameter of disc (m)
D_o	outer diameter of disc (m)
n	speed of rotation (r/min)
p	pressure (Pa)
r	radial distance from centre of point of interest (m)
r_d	radius ratio
R	radius of rotor (m)
S_m	source term (kg)
t	time (s)
Th	aerofoil profile thickness (m)
$\boldsymbol{v}$	velocity vector (m/s)
$\boldsymbol{v}_r$	relative velocity vector (m/s)
V_{rel}	relative velocity magnitude (m/s)
$\bar{V}_{rel}$	non-dimensional relative velocity magnitude
X_{cmax}	position along chord of maximum camber (m)
α	circumferential distance between pins of point of interest (m)
α'	non-dimensional channel width
α_0	Total circumferential distance between pins (m)
μ	viscosity (Pa s)
ρ	density (kg/m^3)
ω	angular velocity (rad/s)
$\boldsymbol{\Omega}$	angular velocity vector (rad/s)